

Locomotion of Active Polymerlike Worms in Porous Media

R. Sinaasappel,¹ M. Fazelzadeh,² T. Hooijschuur,^{1,2} S. Jabbari-Farouji,^{2,*} and A. Deblais^{1,†}

¹*Van der Waals-Zeeman Institute, Institute of Physics, University of Amsterdam, 1098XH Amsterdam, The Netherlands.*

²*Institute for Theoretical Physics, University of Amsterdam, Science Park 904, 1098XH Amsterdam, The Netherlands.*

(Dated: July 29, 2024)

We investigate the locomotion of thin, living *T. Tubifex* worms, which display active polymerlike behavior, within quasi-2D arrays of pillars with different spatial arrangements and densities. These active worms spread in crowded environments, with a dynamics dependent on both the concentration and arrangement of obstacles. In contrast to passive polymers, our results reveal that in disordered configurations, increasing the pillar density enhances the long-time diffusion of our active polymer-like worms, while we observe the opposite trend in ordered pillar arrays. We found that in disordered media, living worms reptate through available curvilinear tubes, whereas they become trapped within pores of ordered media. Intriguingly, we show that reducing the worm's activity significantly boosts its spread, enabling passive sorting of worms by activity level. Our experimental observations are corroborated through simulations of the tangentially-driven polymer model.

Biological organisms exhibit a diverse array of features to optimize their survival strategies and effectively navigate through their disordered natural habitats [1–8]. From actin filaments in the cytoskeleton to larger-scale examples like cyanobacteria in lakes or earthworms in soil, active filaments are observed moving through complex and crowded environments. However, despite their abundance and importance, the mechanisms by which motile filaments navigate through porous media remain poorly understood [9–11].

Few, mostly theory-based modeling studies have been performed on the dynamics of active filaments in complex environments [12–17]. These investigations have predominantly focused on active Brownian and tangentially driven polymer models, delving into the interplay of length, flexibility, and activity on polymer dynamics, both within porous media [15–18] and confined spaces [19]. In the case of active stiff or semi-flexible polymers, they move through the porous medium smoothly with motion that closely resembles reptation, a concept originally elucidated by de Gennes for passive a polymer performing wormlike displacements in arrays of fixed obstacles [20]. In the case of very flexible active polymers however, they will bundle up inside the pores, causing hopping-trapping dynamics where the polymers are stuck in the pores and only rarely hop between pores [17, 18]. In these investigations, the effect of porous medium density and particularly the geometry of the pattern on the dynamics of active polymers has received little attention. Additionally, accurate modeling of migration for active polymers in porous media has been limited because of a lack of suitable experimental model systems to investigate these questions.

In this study, we use *T. Tubifex* worms, which exhibit behavior resembling that of active polymers [21–24], to investigate locomotion within quasi-2D porous media consisting of cylindrical pillars. Comparisons are made with a computational model of tangentially driven active filaments, commonly used to represent self-propelled biopolymers [17, 18, 25]. Our re-

sults reveal the dynamics of the worms depend on the surface fraction ϕ occupied by the pillars and the degree of order in obstacle arrangements. In disordered pillar arrays, the long-time diffusion coefficient D_l increases significantly with ϕ , whereas in square-lattice arrangements, the opposite trend is observed. This transport enhancement in disordered media is attributed to the worms' ability to reptate through accessible curvilinear tubes as formed by randomly positioned pillars, contrasting with their entrapment within voids in ordered configurations. Surprisingly, reducing the worm's activity boosts its spread in disordered media due to an increase in its effective persistence length, which facilitates persistent trajectories within available tubes. Furthermore, our simulations confirm that modeling the worms as tangentially driven active filaments accurately accounts for the long-time dynamics observed in *T. Tubifex* worms.

When deposited on a free surface, the wiggling motions of

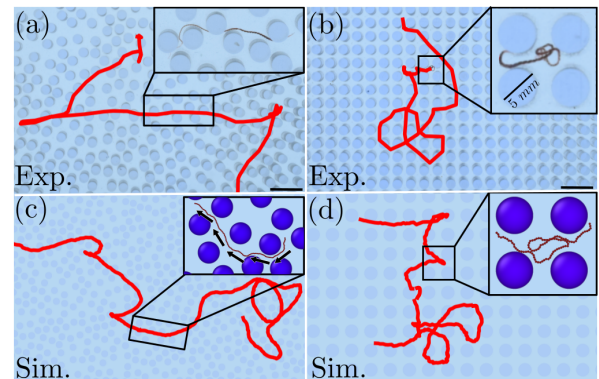


FIG. 1. Trajectories of the center of mass of an active polymerlike worm in $L^2 = 44 \times 44 \text{ cm}^2$ 2D array of pillars with a diameter of 5 mm and surface fraction $\phi = 0.4$ (only a part of medium is shown) in (a) random packing and (b) square lattice for a duration of 185 s; scale bar corresponds to 15 mm. Close-ups show the distinct conformations of a worm arising in the two different obstacle arrangements. (c),(d) Center-of-mass trajectories and representative polymer conformations of the simulated tangentially driven active filaments in the same geometries as in (a),(b).

* s.jabbarifarouji@uva.nl

† a.deblais@uva.nl

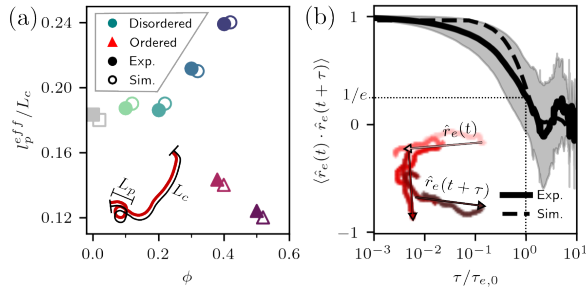


FIG. 2. (a) Effective persistence length l_p^{eff}/L_c of living worms versus tangentially driven active polymer as a function of ϕ . (b) Time auto-correlation function of the end-to-end vector, determining the reorientational relaxation time $\tau_{e,0}^0$ of the worm (continuous line, $\tau_{e,0} \sim 40s$) and of the tangentially driven polymer (dotted lines) in free space.

the *T. Tubifex* allow the worm to crawl on the surface, giving rise to a diffusive motion. The crawling motion is effectively two-dimensional (2D), since the worms are denser than water and, therefore, always located at or close to the bottom part of the geometry.

In our experiments, we introduced a single *T. Tubifex* worm in arrays of pillars with radius $R_p = 2.5$ mm on a two-dimensional square surface 44×44 cm² of the same material which is immersed in a thermostated water volume and we tracked its motion in real time by recording videos for a duration of 2 hours. We investigate locomotion of worms at room temperature $T = 21^\circ\text{C}$ in two distinct pillar arrangements. In the first one, the worms are dispersed in a periodic (square lattice) structure. In the second arrangement, we create a disordered array of pillars by randomly distributing N static pillars with the geometric constraint that the pillars do not overlap. The minimum distance between any two pillars is set to the characteristic width of a worm (approx. 0.5 mm) to ensure that worms can pass through; see Sec. I and Fig. S1 and Fig. S2 in the Supplementary Materials [26] for details. We varied the pillar surface fraction in the range $[0.1, 0.6]$. All the reported conformational and dynamical features of worms at $T = 21^\circ\text{C}$ have been obtained by averaging at least 30 worm trajectories selected with a constant contour length $L_c = 23 \pm 8$ mm; we checked that the contour length does not play a significant role within this range (Sup. Fig. S3, [26]).

In Figure 1, we show typical trajectories of the center-of-mass of a worm moving in a disordered (a) and ordered (b) pillar arrays. In both geometries, as time progresses, the worm is able to navigate through the obstacles but the dynamics with which they do so is found to be dependent on the lattice order and density. To investigate the similarities with active polymers, we conducted simulations using the tangentially-driven polymer model, as described in [17, 27] (see also Sec. II in Sup. Mat. [26]). The motion of each monomer follows overdamped Langevin dynamics, including the active force of amplitude f^a per monomer along the tangent of the backbone of the polymer and the bending stiffness κ between neighboring bonds, which represents the inherent flexibility of the active polymer. The key parameters of the model thus boil down to

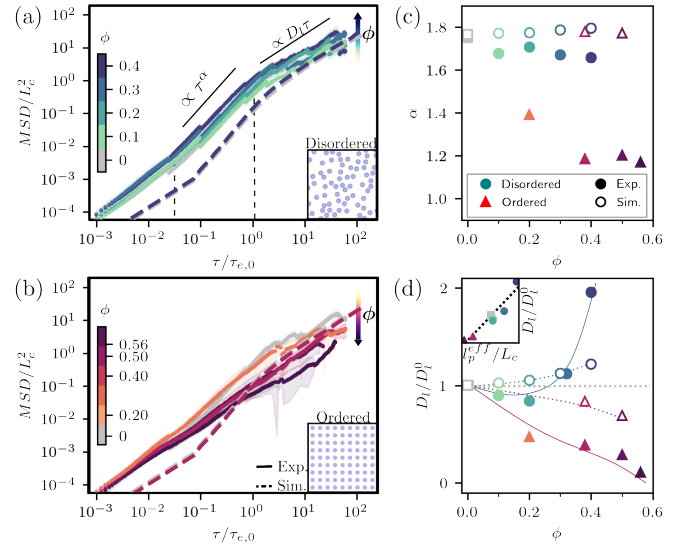


FIG. 3. Mean square displacements (MSD) normalized by contour lengths l_c as a function of time normalized by reorientational time of end-to-end vector $\tau_{e,0}$ for living worms in water at $T = 21^\circ\text{C}$ in disordered (a) and ordered (b) obstacle arrangements. In the disordered pattern (a), the MSD increases faster as surface fraction ϕ rises, while the reverse trend is observed in the ordered pattern (b). Dashed lines represent simulations of the tangentially driven model for $\phi = 0$ (free) and 0.4. (c) The slopes α of the MSD curves in the intermediate regime for both living worms (filled) and simulations of active polymers (open) in both geometries. (d) The long-time diffusion coefficient D_L , normalized with the diffusion coefficient in free space D_L^0 , as a function of ϕ . Lines guide the eyes. The inset shows the linear relationship between D_L and l_p^{eff}/L_c .

(f^a , κ). To compare the tangentially driven polymers to the worms we measure their tangent-vector orientational correlations and average over time (Sup. Fig. S4& S5, [26]). From this we extract the effective persistence length l_p^{eff} , which correlates to κ . The effective persistence length l_p^{eff} is shown by bold symbols in Fig. 2(a) as a function of ϕ in ordered and disordered media, which shows an increase (decrease) with ϕ for worms in ordered and disordered media. Then, we adjust the parameter κ in our simulations to match the observed l_p^{eff} , see the open symbols in Fig. 2(a).

The active force f^a is selected to ensure it dominates at the level of the whole polymer while still allowing thermal fluctuations to affect individual monomers. To compare experiments and simulations, we rescale the time by the reorientational relaxation time of the worm, determined from the $(1/e)$ -decay time of the autocorrelation function of the end-to-end vector, see Fig. 2(b). For tangentially driven polymers in free space with sufficiently large active force ($f^a > 0.01$), both long-time diffusion, dominated by activity, and the orientational relaxation time of the end-to-end vector (τ_e) scale linearly with active force per monomer (f^a). Therefore, rescaling the time by τ_e eliminates the explicit dependence on the active force, making the precise value of f^a less critical [28, 29].

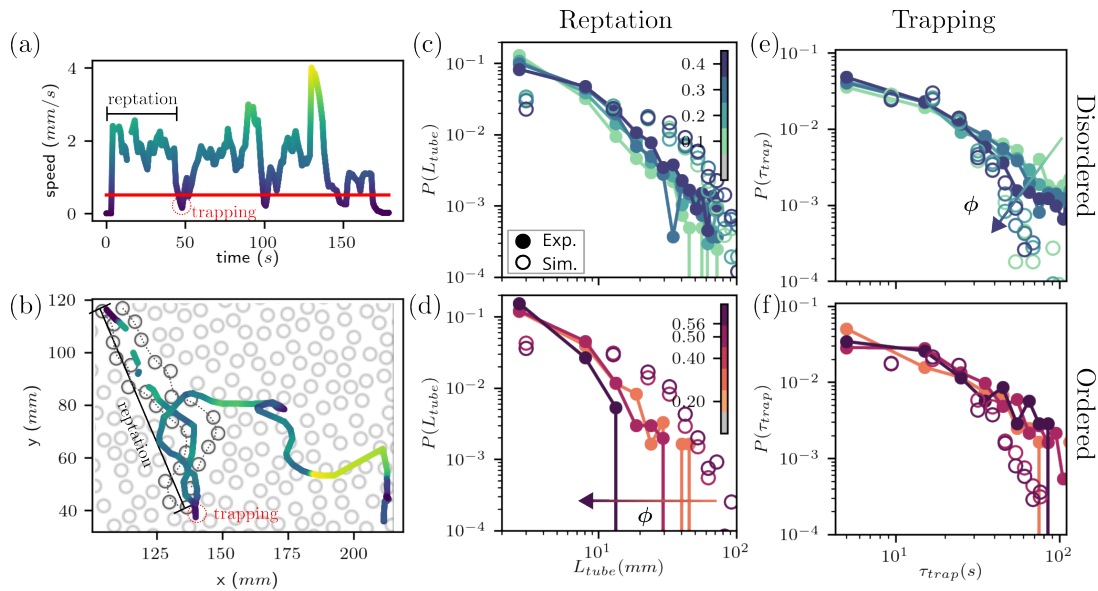


FIG. 4. (a) Example of a worm trajectory ($\phi = 40\%$) as it reptates within an effective tube made by the disordered positioning of pillars. (b) Worms are defined as caged when their instantaneous speed drops below a cutoff of 0.5 mm/s . Between caging events, worms crawl effective tubes of length L_{tube} . (c) and (d) Distribution of tube lengths for disordered (c) and ordered (d) media. Longer tube lengths are observed as ϕ increases in the disordered case, while the maximum tube length decreases for higher ϕ in the ordered medium. The opposite trend is observed for the distribution of trapping times in the disordered (e), and ordered media (f). Open symbols are results from simulations.

We examine the effect of the geometry of the obstacle arrays and the concentration of the pillars on the motion of a self-locomoting worm by measuring the mean squared displacement (MSD) as shown in Figure 3(a) and (b). The time is non-dimensionalized by normalizing with the worm's re-orientational relaxation time in a free environment $\tau_{e,0} \approx 40 \text{ s}$. For short time scales ($\tau/\tau_{e,0} \leq 0.02$), the worms have not yet encountered the pillars, resulting in only slight superdiffusive behavior with a diffusion exponent of 1.2. After this typical time scale, our living worms interact with the pillars with a dynamics that depends on the degree of environmental order. In the disordered case, we observe an almost ballistic regime as shown by $\alpha \sim 1.8$ in Fig. 3(a), which we found to be almost independent of the surface fraction of the pillar ϕ [Fig. 3(c)]. At long times $\tau/\tau_{e,0} \gg 1$, each MSD curve exhibits a diffusive regime where $MSD = 4D_l t$, with a slope that surprisingly increases with ϕ . For the ordered media [Fig. 3(b)], the opposite trend is observed: We observe a weak superdiffusive regime and almost a direct crossover from short-time dynamics to the diffusive regime with a slope that decreases with increasing ϕ . As a result, the presence of an intermediate regime of superdiffusion depends on the arrangement of obstacles, whether they are ordered or not.

The spatial arrangement and density of obstacles influence the long-time diffusion coefficient D_L of the active worms. As shown in Fig. 3(d), the two geometries exhibit opposite effects: in disordered media, D_l increases with ϕ , while it decreases in ordered media, obeying the intuitive expectation that greater crowding slows diffusion. Interestingly, the time scales $\tau \sim \tau_{e,0}$, at which we observe the diffusive regime, do not appear to depend on the obstacle surface fraction ϕ . More-

over, extracting $\tau_e(\phi)$ from the orientational-time autocorrelation of the end-to-end vector (see Sup. Fig. S6 in [26]) confirms that τ_e is independent of ϕ , consistent with simulation results for semiflexible active polymers in periodic obstacle arrays [17].

Examining the trajectories of the worm's center of mass in ordered and disordered pillar arrays, shown in Figs. 1(a),(b), suggests that the contrasting trends in diffusion originate from distinct locomotion strategies. In disordered media, worms and active polymers, see Figs. 1(a),(c), move through effective tubes formed by randomly positioned pillars. They switch between these tubes after brief trapping periods, similar to the reptation of thermal polymers in crowded disordered environments [20, 30–32], where each pore acts as an entropic trap. Between runs, worms become trapped in the pores of the geometries by coiling up, as depicted in Fig. 1(b). Conversely, in the ordered structure, worms appear more flexible, as shown by the lower persistence length in Fig. 3(e). They spend more time within the pores and occasionally hop from one pore to another, with elongated trajectories within narrow throat regions.

This is reflected in the distributions of the curvilinear tube length within which worms and active polymers reptate and their trapping times. Trapping events are determined as the time intervals in which the instantaneous speed of the center of mass drops below $v = 0.5 \text{ mm/s}$, and the trajectory of the center of mass is localized in space; see Figs. 4(a),(b). We define a tube length L_{tube} as the distance a worm travels between trapping events, corresponding to ballistic-like motion within curvilinear tubes formed by the adjacent obstacles. Figs. 4(c),(d) shows the probability distribution function

of the tube run length $P(L_{tube})$ as the worms reptate through available curvilinear tubes. In disordered media, higher pillar densities correlate with longer run lengths within reptation tubes, as evidenced by the larger $P(L_{tube})$ in the tail of the distribution in Fig. 4(c). In contrast, in ordered media, increasing ϕ results in shorter available tube lengths, as reflected by the decrease of $P(L_{tube})$ in the tail with ϕ in Fig. 4(d).

Next, we examine the distribution of trapping times τ_{trap} , defined as the duration of trapping events. Figs. 4(e),(f) show $P(\tau_{trap})$ as a function of τ_{trap} for disordered and ordered media, respectively. In disordered media, the tails of the distribution decrease with increasing ϕ , consistent with our observation that worms spend more time in tubes in this configuration [Fig. 4(e)]. However, in ordered media, the distribution remains almost unchanged with increasing ϕ [Fig. 4(f)]. Our tangentially driven model (open symbols) captures the general shape of the distributions but not the exact dependence on ϕ . These findings invite further scrutiny for both modeling and experiments. Note that the ordered geometry at $\phi = 0.5$ is a hexagonal lattice with a few defects rather than a square lattice, leading to a non-monodisperse void size distribution with a small log-normal contribution. For clarity, these points are omitted from the figure but are shown in Sup. Fig. S7.

The contrasting trends in both the dependence of the long-time diffusion coefficient and the distribution of the run length within tubes on the pillar packing fraction ϕ for ordered and disordered media originate from changes in the effective persistence length of the worms with increasing ϕ . The active contribution to long-time diffusion (D_l^a) is dominant, and theoretical calculations for tangentially-driven active chains predict that it scales as $D_l^a = f^{a2} \langle R_e^2 \rangle \tau_e / (\gamma^2 L_c^2)$, irrespective of ϕ [17], also valid in free space [28, 29] (with the average end-to-end distance $\langle R_e^2 \rangle$ and friction coefficient γ). Additionally, $\tau_e \sim L_c / f^a$ leads to $D_l^a \sim f^a \langle R_e^2 \rangle / L_c$. For the worms, the contour length L_c and the friction coefficient γ do not change. Experimentally measured values of τ_e remain constant regardless of variations in ϕ . Assuming the worm's activity level f^a does not depend on the geometry, changes in $\langle R_e^2 \rangle$ in porous media determine the long-time diffusion. While accurately measuring $\langle R_e \rangle$ experimentally is challenging, we can find a value if we assume the worm-like-chain model for our semiflexible polymer-like worms; $\langle R_e^2 \rangle = 2l_p^{eff} L_c$ when $l_p^{eff} \ll L_c$. Thus, we expect $D_l \sim l_p^{eff}$, as confirmed in the inset of Fig. 3(d).

However, it is worth noting that the tangentially-driven polymer model does not fully capture detailed dynamics, such as the exponent of anomalous diffusion in intermediate regime of MSD as depicted in Fig. 3(c). To achieve complete agreement between experiments and theory, alternative theoretical models are necessary that allow for heterogeneous or time-dependent active force distributions or transversal motion modes [33–36].

Finally, we examine the impact of activity on worm transport, adjustable via ambient water temperature [22]. The average persistence length of worms remains unchanged with temperature [23], whereas their long-time diffusion coefficient (D_l) increases, and their reorientational time (τ_e) decreases with temperature [22]. This behavior aligns with tangentially-driven active polymers, where D_l scales linearly with activity

force (f^a) and τ_e scales as L_c / f^a [28, 29]. Thus, we expect the mean squared displacement (MSD) versus time, scaled by τ_e^T , to be temperature-independent. Fig. 5(a) shows the MSD for worms at three activity levels (low, $T = 5^\circ\text{C}$, intermediate, $T = 21^\circ\text{C}$, and high, $T = 30^\circ\text{C}$). While higher temperatures result in larger MSDs, normalizing by τ_e^T largely mitigates this effect (See Sup. Fig. S8, [26] for the same data in lab-units).

In disordered environments, however, the MSD versus rescaled time (τ / τ_e^T) strongly depends on activity level, as shown in Fig. 5(b). Surprisingly, worms with lower activity ($T = 5^\circ\text{C}$) exhibit faster long-time diffusion than those with higher activity ($T = 30^\circ\text{C}$), despite the increase in τ_e at lower temperatures. This suggests that the contrasting trend is not due to increased worm activity in the porous medium at lower temperatures. Interestingly, the effective persistence length of worms in disordered media, averaged over the experimental timescale (Sup. Fig. S9 [26]), increases at lower temperatures from $l_p^{eff} = 0.12$ to 0.6.

To rationalize these experimental findings, simulations are conducted in the same geometry. The active force is kept constant as in previous experiments and the bending stiffness values are selected to match the effective persistence length measured for worms ($30^\circ\text{C} : \kappa = 5.5$, $5^\circ\text{C} : \kappa = 40$, dashed lines). We observe good agreement between worm behavior and simulations of tangentially driven polymers at large timescales for low-activity worms. However, at high temperatures, the tangentially driven model no longer adequately describes worm dynamics. This suggests that worms under low-temperature conditions and confined by pillars, primarily exhibit peristaltic-like motion. Conversely, at higher activity levels, worms exhibit more transversal modes of motion, indicating the necessity for a more refined model to accurately capture their behavior.

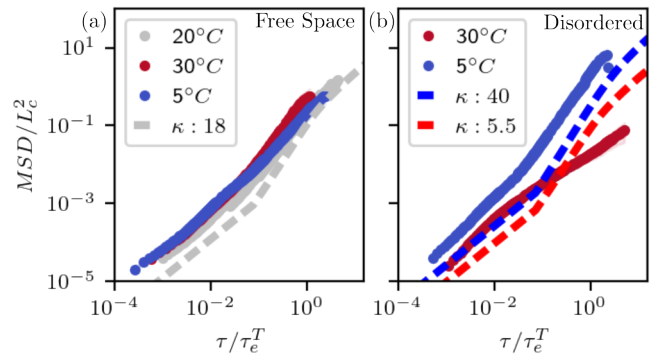


FIG. 5. (a) MSDs of *T. Tubifex* worms at high ($T = 30^\circ\text{C}$, red dots), low ($T = 5^\circ\text{C}$, blue dots) and intermediate ($T = 21^\circ\text{C}$, silver dots) activity levels. Time is normalized by the respective reorientational timescales ($\tau_e^{5^\circ\text{C}} = 78$ s, $\tau_e^{21^\circ\text{C}} = 41$ s, $\tau_e^{30^\circ\text{C}} = 36$ s), which are temperature dependent (Sup. Fig. S9 [26]). Dashed lines show tangentially driven polymer simulations with matching persistence length and $f^a = 0.1$. (b) MSDs of worms at high and low temperatures in disordered porous media. Time is normalized by τ_e^T . At lower temperatures, the effective persistence length increases, enhancing worm spread compared to high temperatures ($T = 30^\circ\text{C}$, red line). Dashed lines correspond to simulation results adjusted for κ .

In conclusion, our study highlights the crucial role of environmental order, porosity, and activity in shaping the dynamics of active flexible agents. Unlike previous work on active stiff and semi-flexible polymers [5, 12], we demonstrate that pore morphology significantly influences the large-scale spreading of living worms. These findings highlight the im-

portance of pore geometry in modulating transport phenomena within porous environments, suggesting potential for manipulation through lattice patterning. Moreover, our observations suggest that strategically distributing active forces along a driven polymer could enhance active transport, analogous to the behaviors observed in our living worms.

-
- [1] K. M. Dorgan, C. J. Law, and G. W. Rouse, Meandering worms: mechanics of undulatory burrowing in muds, *Proceedings of the Royal Society B: Biological Sciences* **280**, 20122948 (2013).
- [2] C. Bechinger, R. Di Leonardo, H. Löwen, C. Reichhardt, G. Volpe, and G. Volpe, Active particles in complex and crowded environments, *Reviews of Modern Physics* **88**, 045006 (2016).
- [3] J. E. Sosa-Hernández, M. Santillán, and J. Santana-Solano, Motility of *escherichia coli* in a quasi-two-dimensional porous medium, *Phys. Rev. E* **95**, 032404 (2017).
- [4] S. Makarchuk, V. C. Braz, N. A. M. Araújo, L. Ciric, and G. Volpe, Enhanced propagation of motile bacteria on surfaces due to forward scattering, *Nature Communications* **10**, 4110 (2019).
- [5] T. Bhattacharjee and S. S. Datta, Bacterial hopping and trapping in porous media, *Nature Communications* **10**, 2075 (2019).
- [6] A. Kudrolli and B. Ramirez, Burrowing dynamics of aquatic worms in soft sediments, *Proceedings of the National Academy of Sciences* **116**, 25569 (2019), publisher: Proceedings of the National Academy of Sciences.
- [7] A. Dehkharghani, N. Waisbord, and J. S. Guasto, Self-transport of swimming bacteria is impaired by porous microstructure, *Communications Physics* **6**, 1 (2023).
- [8] G. Juarez, K. Lu, J. Sznitman, and P. E. Arratia, Motility of small nematodes in wet granular media, *Europhysics Letters* **92**, 44002 (2010).
- [9] R. Lux, J. N. Miller, N.-H. Park, and W. Shi, Motility and Chemotaxis in Tissue Penetration of Oral Epithelial Cell Layers by *Treponema denticola*, *Infection and Immunity* **69**, 6276 (2001).
- [10] D. N. Thornlow, E. L. Brackett, J. M. Gigas, N. Van Dessel, and N. S. Forbes, Persistent enhancement of bacterial motility increases tumor penetration, *Biotechnology and Bioengineering* **112**, 2397 (2015).
- [11] B. J. Toley and N. S. Forbes, Motility is critical for effective distribution and accumulation of bacteria in tumor tissue, *Integrative Biology: Quantitative Biosciences from Nano to Macro* **4**, 165 (2012).
- [12] L. Theyancheri, S. Chaki, T. Bhattacharjee, and R. Chakrabarti, Active dynamics of linear chains and rings in porous media, *The Journal of Chemical Physics* **159**, 014902 (2023).
- [13] T. Majmudar, E. E. Keaveny, J. Zhang, and M. J. Shelley, Experiments and theory of undulatory locomotion in a simple structured medium, *Journal of The Royal Society Interface* **9**, 1809 (2012), publisher: Royal Society.
- [14] Z. Mokhtari and A. Zippelius, Dynamics of active filament in porous media, *Phys. Rev. Lett.* **123**, 028001 (2019).
- [15] C. Kurzthaler, S. Mandal, T. Bhattacharjee, H. Löffwen, S. S. Datta, and H. A. Stone, A geometric criterion for the optimal spreading of active polymers in porous media, *Nature Communications* **12**, 7088 (2021).
- [16] A. R. Tejedor, R. Carracedo, and J. Ramírez, Molecular dynamics simulations of active entangled polymers reptating through a passive mesh, *Polymer*, 125677 (2023).
- [17] M. Fazelzadeh, Q. Di, E. Irani, Z. Mokhtari, and S. Jabbari-Farouji, Active motion of tangentially driven polymers in periodic array of obstacles, *The Journal of Chemical Physics* **159**, 224903 (2023).
- [18] Z. Mokhtari and A. Zippelius, Dynamics of active filaments in porous media, *Physical Review Letters* **123**, 028001 (2019).
- [19] J. Martín-Roca, E. Locatelli, V. Bianco, P. Malmaretti, and C. Valeriani, Tangentially active polymers in cylindrical channels (2024), arXiv:2405.02192 [cond-mat.soft].
- [20] P. G. de Gennes, Reptation of a polymer chain in the presence of fixed obstacles, *The Journal of Chemical Physics* **55**, 572 (1971), publisher: American Institute of Physics.
- [21] A. Deblais, S. Woutersen, and D. Bonn, Rheology of entangled active polymer-like t. tubifex worms, *Physical Review Letters* **124**, 188002 (2020).
- [22] A. Deblais, A. Maggs, D. Bonn, and S. Woutersen, Phase separation by entanglement of active polymerlike worms, *Physical Review Letters* **124**, 208006 (2020).
- [23] T. Heeremans, A. Deblais, D. Bonn, and S. Woutersen, Chromatographic separation of active polymer-like worm mixtures by contour length and activity, *Science Advances* **8**, eabj7918 (2022).
- [24] A. Deblais, K. R. Prathyusha, R. Sinaasappel, H. Tuazon, I. Tiwari, V. P. Patil, and M. S. Bhamla, Worm blobs as entangled living polymers: from topological active matter to flexible soft robot collectives, *Soft Matter* **19**, 7057 (2023).
- [25] R. G. Winkler and G. Gompper, The physics of active polymers and filaments, *The Journal of Chemical Physics* **153**, 040901 (2020).
- [26] See Supplemental Material [url] for more details on the experimental methods, set-up and on the simulations of the tangentially-driven polymer model. It includes the references [17, 21, 27, 29, 30, 37, 38].
- [27] R. E. Isele-Holder, J. Elgeti, and G. Gompper, Self-propelled worm-like filaments: spontaneous spiral formation, structure, and dynamics, *Soft Matter* **11**, 7181 (2015).
- [28] M. Fazelzadeh, E. Irani, Z. Mokhtari, and S. Jabbari-Farouji, Effects of inertia on conformation and dynamics of tangentially driven active filaments, *Phys. Rev. E* **108**, 024606 (2023).
- [29] V. Bianco, E. Locatelli, and P. Malmaretti, Globulelike conformation and enhanced diffusion of active polymers, *Phys. Rev. Lett.* **121**, 217802 (2018).
- [30] M. Doi and S. F. Edwards, *The Theory of Polymer Dynamics* (Clarendon Press, Oxford, 1986).
- [31] M. Muthukumar and A. Baumgärtner, Diffusion of a polymer chain in random media, *Macromolecules* **22**, 1941 (1989).
- [32] M. Muthukumar and A. Baumgärtner, Effects of entropic barriers on polymer dynamics, *Macromolecules* **22**, 1937 (1989).
- [33] M. Vatin, S. Kundu, and E. Locatelli, Conformation and dynamics of partially active linear polymers, *Soft Matter* **20**, 1892 (2024).

- [34] S. K. Anand and S. P. Singh, Structure and dynamics of a self-propelled semiflexible filament, *Physical Review E* **98**, 042501 (2018), publisher: American Physical Society.
- [35] S. K. Anand and S. P. Singh, Conformation and dynamics of a self-avoiding active flexible polymer, *Physical Review E* **101**, 030501 (2020), publisher: American Physical Society.
- [36] K. Prathyusha, F. Ziebert, and R. Golestanian, Emergent conformational properties of end-tailored transversely propelling polymers, *Soft Matter* **18**, 2928 (2022).
- [37] J. D. Weeks, D. Chandler, and H. C. Andersen, Role of repulsive forces in determining the equilibrium structure of simple liquids, *The Journal of Chemical Physics* **54**, 5237 (1971).
- [38] K. Binder, S. A. Egorov, A. Milchev, and A. Nikoubashman, Understanding the properties of liquid-crystalline polymers by computational modeling, *Journal of Physics: Materials* **3**, 032008 (2020).

**SUPPLEMENTARY MATERIALS FOR
“LOCOMOTION OF ACTIVE POLYMERLIKE WORMS IN POROUS MEDIA”**

This Supplementary Material provides additional information on the experimental setup and methodologies employed in this study and on the tangentially driven polymer model utilized for our analysis.

I. EXPERIMENTS

A. Experimental set-up

In our experiments, we placed a single *T. Tubifex* worm into pillar arrays submerged in a thermostated water volume, tracking their motion in real-time through 2-hour video recordings. We investigated two geometries: (i) a periodic crystalline structure and (ii) a disordered geometry with randomly positioned pillars.

For each pattern, we inserted N static pillars with a radius $R_p = 2.5$ mm on a square two-dimensional surface of the same material, ensuring no overlap between the pillars. We imposed the condition that the minimum distance between two pillars is approximately the characteristic width of a worm (~ 500 μm) to allow worm passage. The surface fraction of the pillar varied from 10% to 60%, calculated as $\phi = N\pi R_p^2/L^2$. In the disordered medium, pillar positions were randomly selected using the *numpy.random* library in Python. Pillar placement continued sequentially, retrying if a selected location was closer than $2.5+1$ mm to a previously placed pillar, until reaching the desired surface fraction ϕ . Supplementary Figure SS1 shows the experimental geometries, with dimensions L^2 of 230×230 mm² for ordered and 440×440 mm² for disordered setups. The larger setup involved cutting holes in an acrylic sheet and placing short acrylic rods with a radius of 2.5 mm; the ordered geometries were 3D-printed. We observed no significant differences in the behavior of the worm between the two dimensions.

To quantify the size of the voids in the different geometries, we used Delaunay triangulation (as implemented in the *scipy.spatial* library). Delaunay triangulation divides an area containing a set of points into triangles, such that the circum-circles of these triangles do not contain any points. It allows us to find the biggest possible circles that one can draw that do not contain any of the pillars. The radius of these circles are taken as a good approximation for the void sizes in the geometries, so it is possible to compare how the void size distribution changes with the surface fraction of the pillars. Supplementary Figure SS2 shows the distribution of void radii in the pillar arrays, following a log-normal distribution. For larger surface fraction above $\phi = 50\%$, we were unable to produce a disordered medium using the standard method. Instead, we started from an evenly spaced hexagonal lattice, randomly removing pillars to achieve the desired surface fraction. Next, the pillars were allowed to diffuse for a while. This resulted in a (largely) hexagonal lattice with defects, exhibiting a more mono-disperse void size distribution. Due to this, the worms behaved similarly to those in the square lattice geometries, therefore they will be referred to as ordered in subsequent materials.

1. Tracking and mean square displacement (MSD)

In the experiments, worms are positioned atop the geometries in a 15 cm deep water bath, dimly illuminated from below with an LED panel. The camera recordings from above capture the experiments (Nikon D5300 equipped with a macrolens), which are subsequently analyzed using a Python script. From the images, we extracted the center of mass (CoM) and the contour of the worm, as shown in Figure SS4.

After tracking the worm's CoM position ($\mathbf{r} = (x, y)$), we compute the mean square displacement as a function of lag time $\text{MSD}(\tau) = \langle (r(\tau) - r(0))^2 \rangle$. Each experiment yields one MSD curve, which is then averaged to produce the curves reported in the main paper. Supplementary Figure SS3 displays the MSD curves of all experiments with the average represented by the black line.

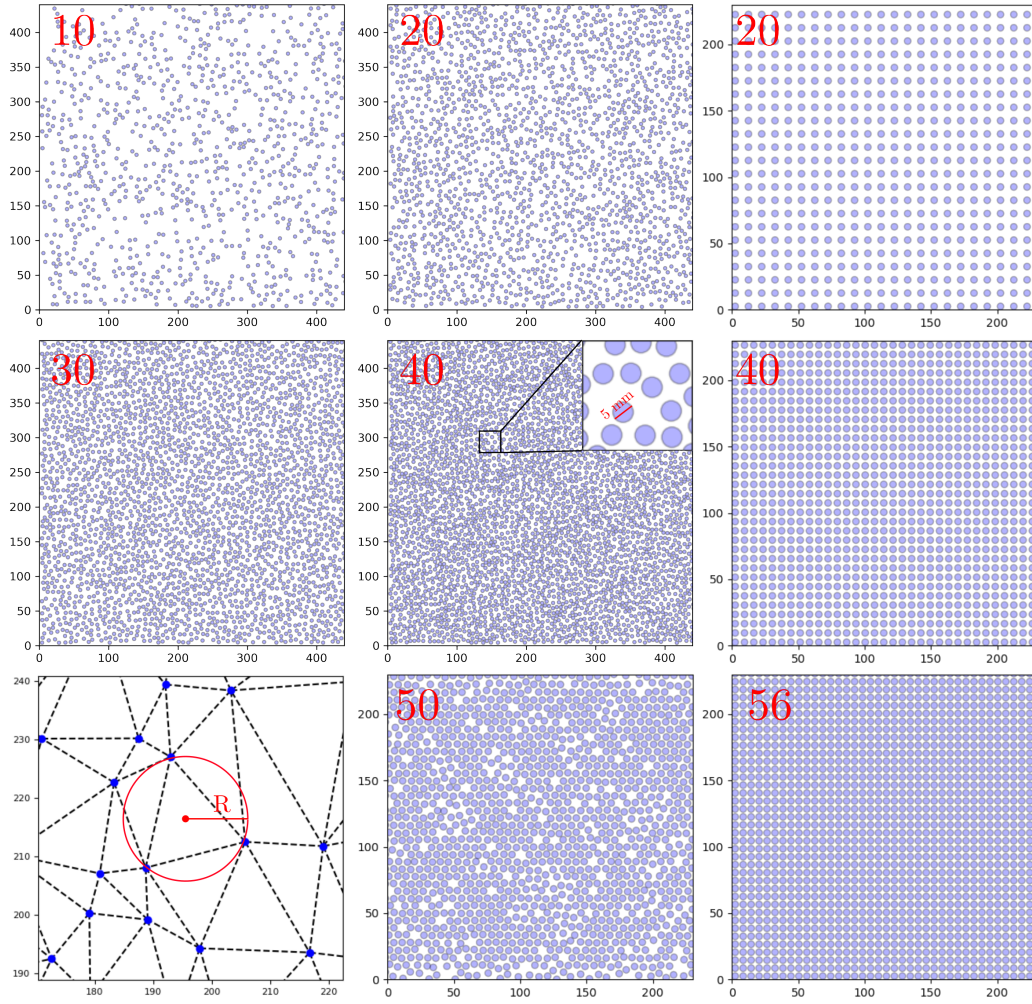


FIG. S1. **The ordered and disordered geometries used in the experiments.** The axis are in millimeters and the radius of the pillars is $r = 2.5$ mm. The surface fraction occupied by the pillars is indicated in the top left corner in red. The bottom left corner shows the Delaunay triangulation.

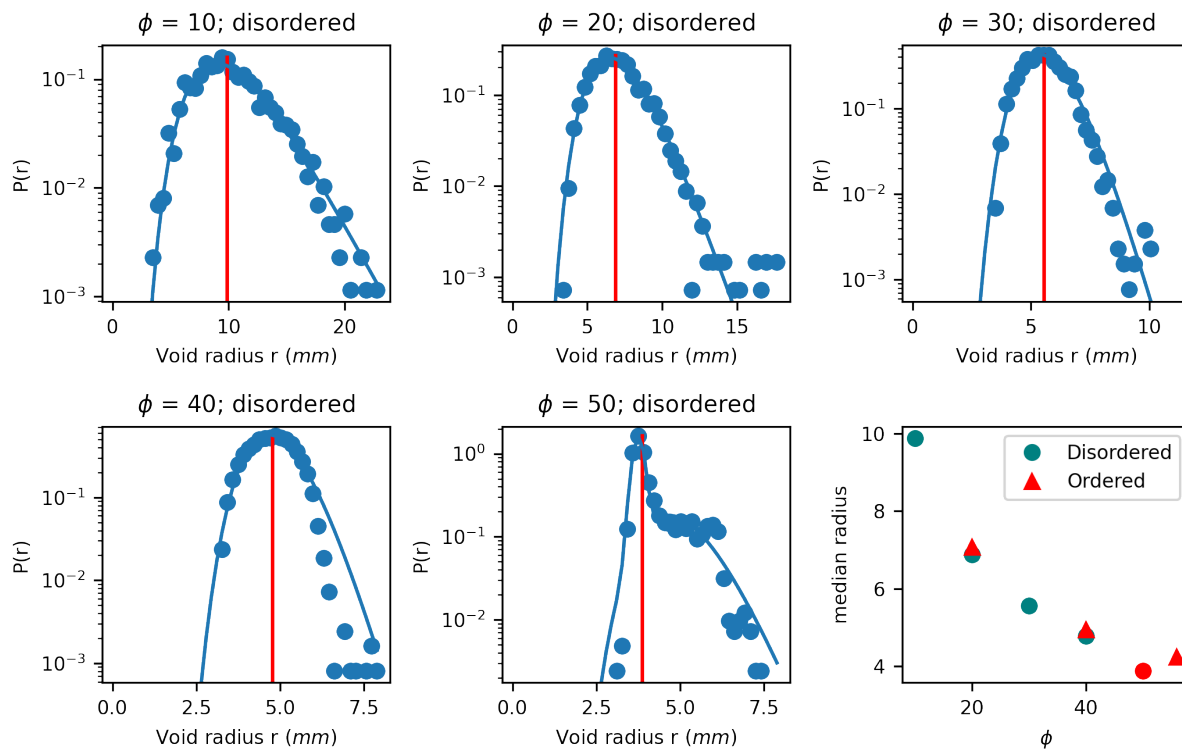


FIG. S2. **Pore size distribution in the geometries.** Distribution of the radii of all possible biggest circles that do not contain any points, as found through Delaunay triangulation, as a measure for the size of the voids in the pillar arrays. The distribution of the void sizes are well fitted with a log-normal distribution. For $\phi = 50\%$ the distribution is fitted by the sum of a Gaussian and a log-normal distribution.

B. Effect of worm's contour length, L_c

In our experiments, worms of varying lengths were used due to experimental constraints (batch of worms are polydisperse in their contour lengths). However, we did not observe any significant correlation between the length of the worms and their behavior. Analysis of the long-time diffusion constant and MSD curves revealed no discernible correlation with the length of the worm, as illustrated in Figure S3(a-f), where the color code represents the contour length of the worm.

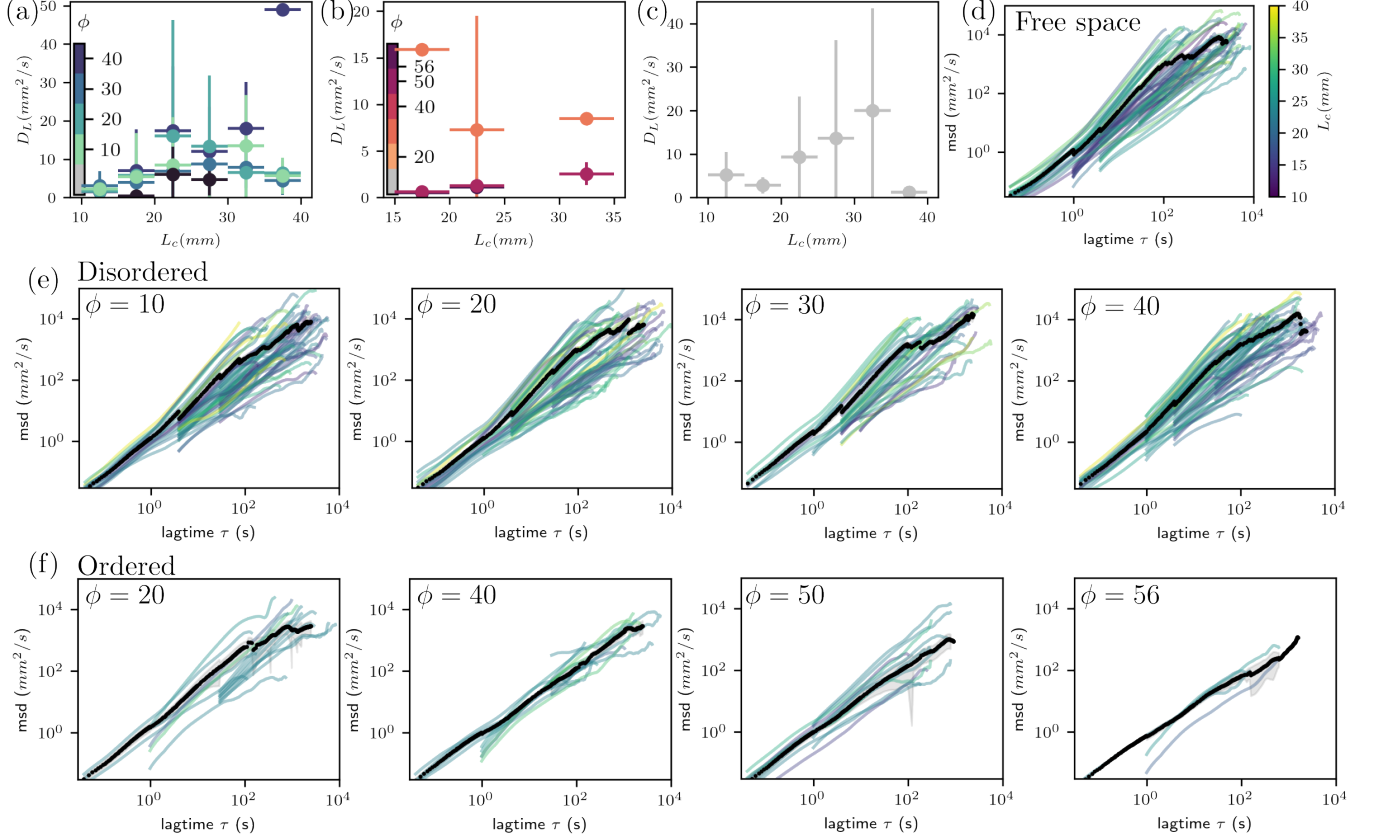


FIG. S3. **MSD curves of all experiments.** (a) Long-time diffusion constant versus the contour length of worms in the disordered, (b) ordered media, and (c) in free space. (d) MSD curves of worms in free space in lab units. The color of the lines indicates the contour length of the worms. The average is indicated by the black line. (e) All MSD curves for the disordered medium. The color of the lines is mapped according to the color bar in (d). The surface fraction of the pillars is indicated in the top left corner. (f) All MSD curves for the ordered medium. The color of the lines is mapped according to the color bar in (d). The surface fraction of the pillars is indicated in the top left corner.

C. Conformation

1. Effect of the geometry and temperature on the persistence length

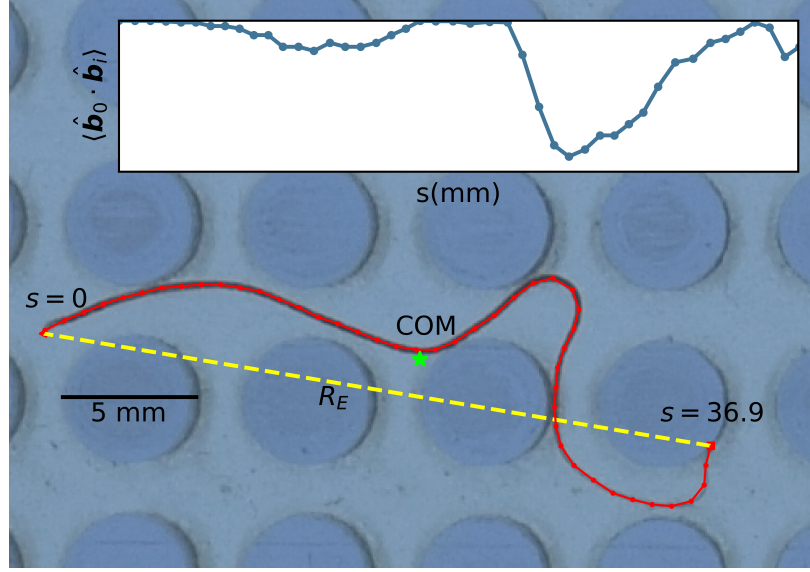


FIG. S4. Determination of the persistence length.

To determine the appropriate bending stiffness κ of the semi-flexible polymers in the simulations, we calculated the effective persistence length l_p^{eff} from the videos of the worms for different surface fractions and in ordered and disordered media. Calculating the persistence length involves defining an effective bond vector for the worm. Firstly, we remove the background from each image and select a smaller region of interest (ROI) of the total image where the worm is either 600×600 or 360×360 pix^2 , depending on the total image size. Within this selected image region, we identify all pixels belonging to the individual worm and employ a skeletonization algorithm to obtain a single-pixel-wide chain of pixels, which forms the initial polymer-like backbone of the worm. Each pixel can be regarded as a monomer, with neighboring pixels connected by bond vectors $\mathbf{r}_{i,j}$.

However, at the single-pixel level, each neighbor has only 8 possible directions it can be connected, resulting in discrete bond vectors and sharp lines in the bond-bond correlation function. Additionally, at high resolution, each pixel represents a minute scale, rendering the bonds effectively rigid, leading to a plateau in the bond-bond correlation. To address these issues, we average every four pixels to create a new monomer \mathbf{r}_i^* , and these are connected by new bond vectors, denoted as \mathbf{b}_i , where i ranges from 0, the first bond in the chain, to $i = N - 1$, the last bond.

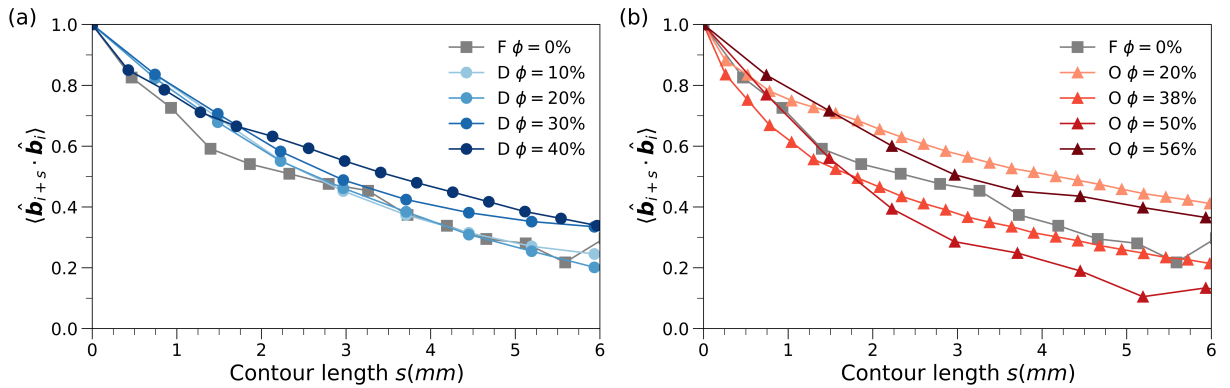


FIG. S5. Effect of the lattice pattern on the persistence length. (a) Bond-Bond correlation of the worms in the disordered medium. The persistence length increases with increasing the packing fraction (b) The effect of the increasing packing fraction in a ordered arrangement on the persistence length. The bond-bond correlation curves are averaged in time over around 10 minutes of footage per worm for 5 different worms.

To determine the bond-bond correlation function, we examine the dot product between a normalized bond vector $\hat{\mathbf{b}}_i$ at the point i and a bond vector s that bonds along the chain $\hat{\mathbf{b}}_{i+s}$. This dot product yields an angle $\cos(\theta)$ between the bonds, which decreases as we move along the contour s until it becomes completely uncorrelated at $\cos(\theta) = 0$. In molecular dynamics simulations of polymers, this decay follows a decreasing exponential pattern, given by $\langle \hat{\mathbf{b}}_{i+s} \cdot \hat{\mathbf{b}}_i \rangle = e^{-s/l_p}$, where l_p represents the persistence length of the worm. The averaging $\langle \dots \rangle$ involves both a time and a sample average, incorporating different frames of the same worm, as well as averaging over trajectories of different worms.

To extract the persistence length from the bond-bond correlation function, we fit the exponential function to the data for the first 5 mm of the worm contour. Long-range correlations are less accurate because of fewer frames in which the entire worm is visible, often caused by overlaps or obstructing pillars. An alternative method is to use the crossing point of $\langle \hat{\mathbf{b}}_{i+s} \cdot \hat{\mathbf{b}}_i \rangle$ at $1/e$, but for very stiff worms, this crossing point may not always be reached for high contour lengths. By focusing solely on the first 5 mm of the contour, this issue is mitigated, and the data are less noisy at these data points. In figure SS5 the bond-bond correlation curves are reported.

2. Effect of the geometry on τ_e and R_e

In order to use the prediction for the long-time diffusion of tangentially driven chain [17], we determine the average end-to-end distance R_e and the reorientational decorrelation time τ_e , both obtained from the detection and tracking of the worm's contour as mentioned above. Sup. Figs.S S6(a)-(c) show the orientational correlation in time, the average reorientational decorrelation time and the average end-to-end distance of the worms across all geometries, respectively. It is notable that we observe no significant dependence of the pillar surface fraction ϕ on τ_e , while only a weak dependence is observed for R_e . This discrepancy may seem surprising, especially given the strong dependence of the persistence length of the worm on ϕ (as discussed in Section C1 above and depicted in Fig. 2(a) of the main text). However, this inconsistency can be attributed to the difficulty of accurately measuring R_e and τ_e when parts of the worm are obscured by the pillars. Unlike the tracking of the center of mass and the determination of the persistence length, which remain well defined despite partial obstruction, identifying the endpoints of the worm's skeleton for R_e and τ_e measurements can be difficult when obscured by the pillars.

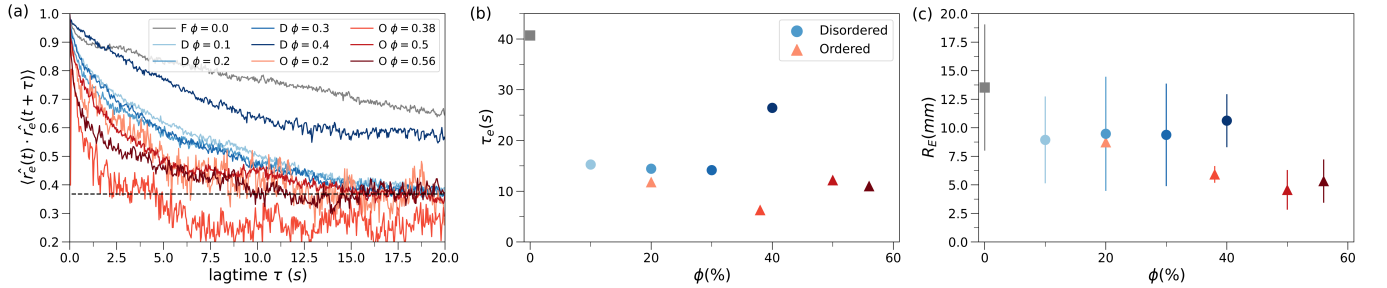


FIG. S6. Effect of the lattice geometry on τ_e and R_e . (a) The orientational correlation in time, (b) the average reorientational decorrelation time and (c) the average end-to-end distance of the worms across all geometries.

D. Locomotion

1. Run lengths and trapping times

In the main text, we excluded the points for the ordered lattice at 50% because the data for this experiments deviates slightly from the trend. The reasons why are easily explained, but distract from the main point of the figure. The ordered lattice at 50% has a non-monotonous pore size distribution because this is a slightly noisy hexagonal lattice with a few removed pillars (see figure SS1&SS2). The worms still show hopping-trapping behavior where they hop through very short tubes between pores, but the worms are sometimes able to find longer tubes while simultaneously having longer trapping times. In figure S7 the values of the run length and trapping times of this data are reported

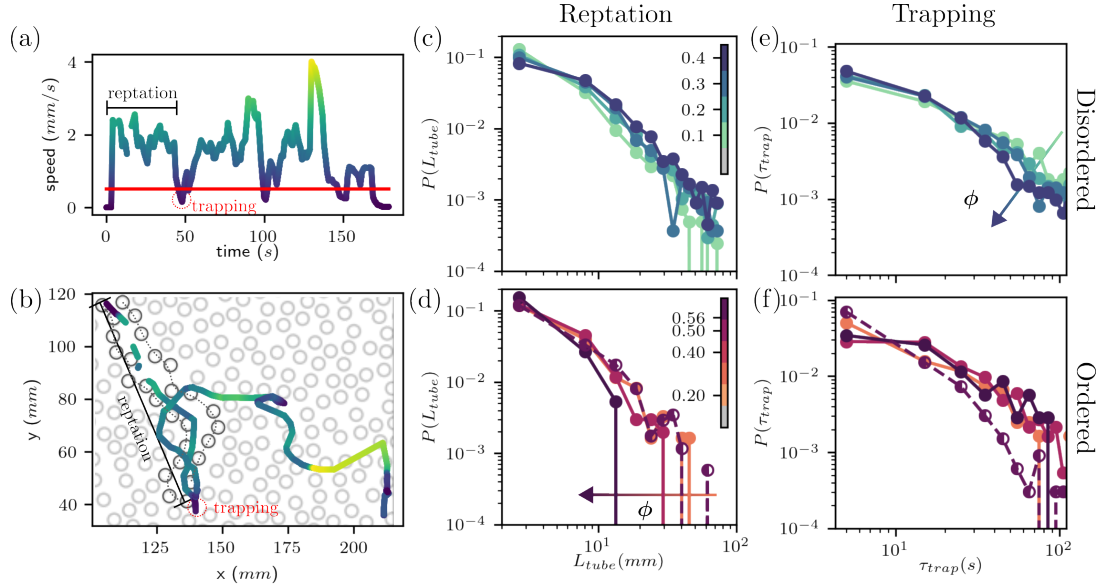


FIG. S7. **Tube length and trapping time distributions** (a) Worms are defined as caged when their instantaneous speed drops below a cutoff of 0.5 mm/s . Between caging events, worms crawl effective tubes of length L_{tube} . (b) Example of a worm trajectory ($\phi = 40\%$) as it reptates within an effective tube made by the disordered positioning of pillars. (c) and (d) Distribution of tube lengths for disordered (c) and ordered (d) media. Longer tube lengths are observed as ϕ increases in the disordered case, while the maximum tube length decreases for higher ϕ in the ordered medium. The opposite trend is observed for the distribution of trapping times in the disordered (e), and ordered media (f). The half-open symbols correspond to the ordered lattice at $\phi = 50\%$.

2. Effect of temperature

When placed in warmer water, our living worms become more active, resulting in faster motion and increased shape's fluctuation rates. In free space, their long-time diffusion increases with temperature [21]. However, in dense disordered media, both the long-time diffusion time and the reorientational relaxation time decrease at higher temperatures. This occurs because the worms become trapped in cavities more frequently, preventing them from being stretched out long enough to initiate reptation. This trend is also evident in the effective persistence length of the worms. See figure SS8 for the MSD curves in laboratory units, Figure SS9 (a) for the persistence length and figure SS9(b) for the calculation of the reorientational relaxation time.

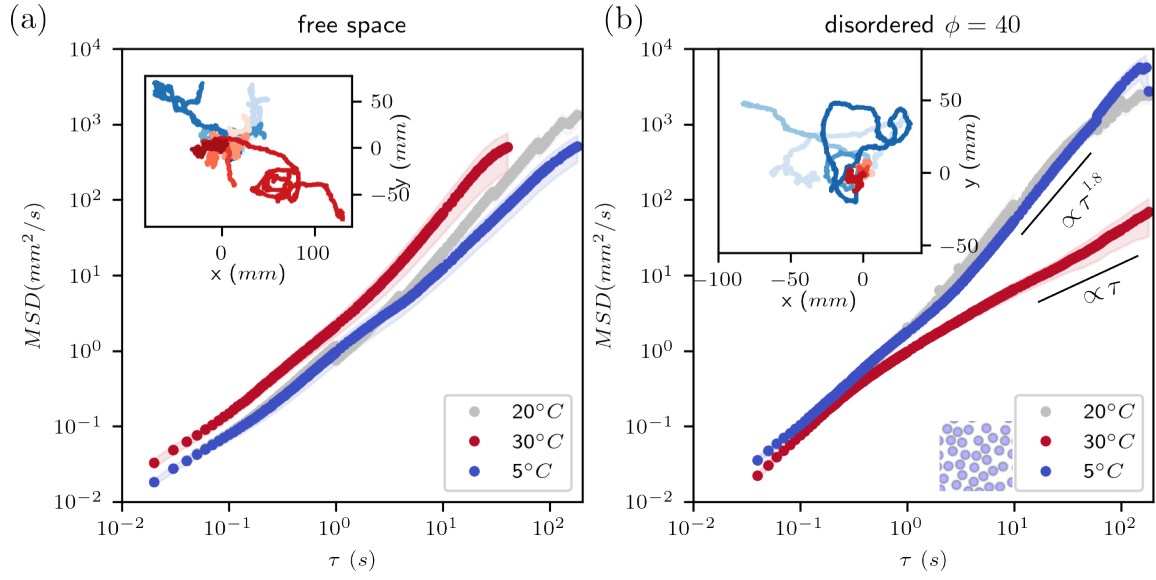


FIG. S8. **MSD for the same set of worms at different temperatures in lab units.** a) Worms in free space. The hotter the worms, the more active they are and the higher their MSD-curves b) Worms in $\phi = 40\%$ disordered porous media. The cold worms show strong reptation (even stronger than worms at room temperature), while the worms in a 30°C bath never reptate and show purely diffusive hopping-trapping behavior.

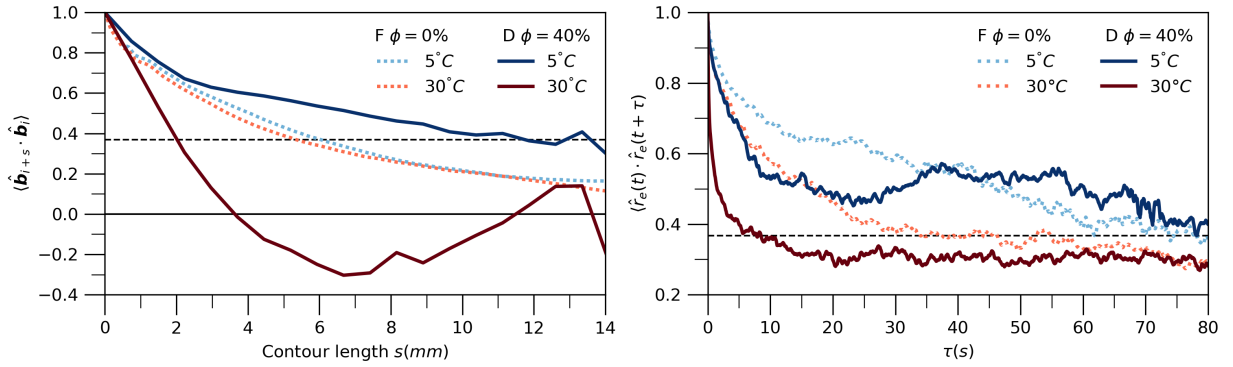


FIG. S9. **Dependence of l_p and τ_e on the temperature** a) bond-bond correlation for worms at 5°C (blue) and 30°C (red) as a function of time in free space (dotted lines) and the disordered media at $\phi=40\%$ (solid lines). The intersection with the black dashed line at $1/e$ defines the persistence length. b) Orientational correlation for worms at 5°C (blue) and 30°C (red) as a function of time in free space (dotted lines) and the disordered media at $\phi=40\%$ (solid lines). The intersection with the black dashed line at $1/e$ defines the reorientational relaxation time.

3. Bimodal distributions in the disordered geometries

Here we would like to zoom in a bit more on the trajectories and subsequent MSD curves of the worms in the disordered geometries. Interestingly, distinct trajectories emerge in our experiments, segregating into two populations across all obstacle densities. One population showcases elongated, ballistic stretches as the worms reptate from one tunnel to another. In contrast, the second population exhibits hopping behavior, crawling from cavity to cavity with purely diffusive dynamics. As the obstacle density increases, the likelihood that a worm belongs to the ballistic population also increases. Consequently, the long-time diffusion constant increases when averaging over all trajectories from both populations, as illustrated in Figure SS10. In the top panel of the figure, for each maze configuration, the trajectories are segregated into two populations using a cutoff at the intermediate slope of each trajectory. It is evident that the worms exhibit ballistic and diffusive motion within each maze. However, as depicted in the PDFs in the bottom panels, there is a notable shift in behavior, with worms transitioning from a preference for diffusive motion to a preference for ballistic movement as obstacle density increases. This shift is attributed to the worm's capacity to reptate through effective tubes mapped out by the position of the pillars. It is worth noting here that the same individual worms were tested across all mazes, indicating behavioral changes in individual worms.

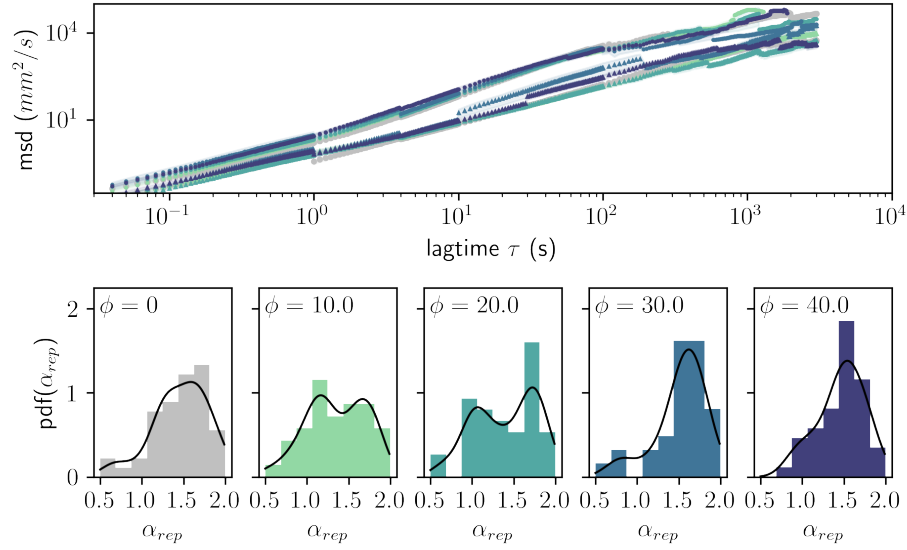


FIG. S10. **average MSD curves and slope distribution for the disordered media** For the disordered maze, some worms travel in large ballistic stretches, while some worms move along a diffusive trajectory. The probability of a worm moving ballistically increases if the worm is in a more crowded environment (e.g., higher ϕ).

II. SIMULATIONS

A. Tangentially-driven polymer model

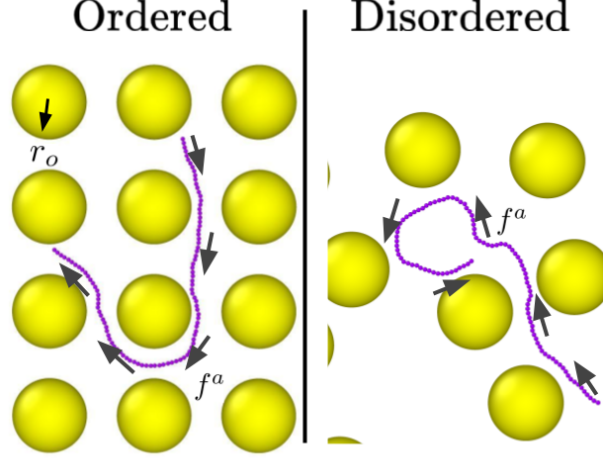


FIG. S11. Schematic of the active tangentially-driven polymer in the ordered and disordered arrangement of obstacles.

We implement the tangentially-driven polymer model [27] into both a 2D ordered and disordered arrangement of circular obstacles, as illustrated in Sup. Fig.S S11. In our experimental setup, we observe the 2D projection of 3D active filaments around cylindrical pillars, indicating that the polymer can intersect with itself. To take into account this behavior, we neglect excluded volume interactions between monomers, and instead, we consider a phantom active polymer model comprising N monomers. The motion of each monomer follows overdamped Langevin dynamics, described by:

$$\gamma \dot{\vec{r}}_i = - \sum_j \nabla_{\vec{r}_i} U + \vec{f}_i^a + \vec{f}_i^r, \quad (1)$$

where \vec{r}_i is the position of the i th monomer, the dot denotes the derivative with respect to time and γ is the friction coefficient between the bead and its surrounding medium.

The potential energy U of each monomer includes three different contributions. The first one is the harmonic spring potential $U_{\text{harmonic}}(r) = (k_s/2)(r - \ell)^2$, with equilibrium length ℓ and spring stiffness k_s between adjacent monomers. The second part is the bending potential between each two neighboring bonds $U_{\text{bend}}(\theta_i) = \kappa(1 - \cos\theta_i)$, where θ_i denotes the angle between two consequent bonds intersecting at bead i defined as $\theta_i = \cos^{-1}(\hat{t}_{i,i+1} \cdot \hat{t}_{i-1,i})$ with $\hat{t}_{i,i+1} = \vec{r}_{i,i+1}/|\vec{r}_{i,i+1}|$ and $\vec{r}_{i,i+1} = \vec{r}_{i+1} - \vec{r}_i$. Here, κ is the bending stiffness and determines the intrinsic degree of flexibility of a polymer. Finally, the third contribution accounts for the excluded volume interactions between each bead and its surrounding obstacles. They are modeled by the short-ranged Weeks-Chandler-Andersen (WCA) potential [37]:

$$U_{\text{excl}}(r) = 4\epsilon \left[\left(\frac{\sigma/2 + r_o}{r} \right)^{12} - \left(\frac{\sigma/2 + r_o}{r} \right)^6 + \frac{1}{4} \right] \quad (2)$$

for $r < r_c = 2^{1/6}(\sigma/2 + r_o)$, where ϵ is the strength of the potential and has unit of energy, σ is the diameter of the beads and r_o is the radius of obstacles. The WCA potential is zero for interaction distances larger than the cutoff length r_c .

The active force on each bead, except for the end monomers, is given by: $\vec{f}_i^a = \frac{f^a}{2\ell}(\vec{r}_{i-1,i} + \vec{r}_{i,i+1})$. The active force on the tail monomer is given by $\vec{f}_1^a = \frac{f^a}{2\ell}\vec{r}_{1,2}$ and for the head monomer by $\vec{f}_N^a = \frac{f^a}{2\ell}\vec{r}_{N-1,N}$. The random force is chosen as a white noise of zero mean and has the correlation $\langle \vec{f}_i^r(t) \cdot \vec{f}_j^r(t') \rangle = 4D_0\gamma^2\delta_{ij}\delta(t-t')$. It should be noted that the persistence length of a 2D passive ideal polymer in free space can be determined in terms of its bending stiffness and the strength of random force correlation as $l_p^0 = 2\kappa\sigma/D_0\gamma$. [38].

We use the coordinates of the pillars in experiment to position the obstacles in a 2D simulation box with periodic boundary condition. We choose $l_u = \sigma$, $E_u = \epsilon$ and $\tau_u = \gamma\sigma^2/\epsilon$ with $\gamma = 1$ as the units of length, energy, and time. Subsequently, we fix

$\ell = 1\sigma$, $N = 100$, $r_o = 8.33\sigma$ and the diffusion coefficient $D_0 = 1\epsilon/\gamma$. The ratio between the obstacle radius, chain length and monomer diameter is set with respect to the average length and thickness of the worms. We choose an active force of $f^a = 0.1\epsilon/\sigma$ and the spring constants are chosen very stiff $k_s = 5000\epsilon/\sigma \gg f^a/\ell$, to ensure that the mean bond length and the polymer contour length remain almost constant during simulations. It has been well established that the relaxation time of flexible tangentially driven chains in free space scales as $\tau_e \sim 1/f^a$, while their enhanced diffusion coefficient scales as $D_I \sim f^a$ [17, 29]. Hence, when using the relaxation time as the unit of time, the D_I of chains with different activities become identical. Our choice of active force ($f^a = 0.1$), ensures that the activity dominates the motion of the whole polymer chain, but it is weak enough to let the thermal fluctuation affect the chain on monomer level. At the chain level, the thermal relaxation time suggested by the Rouse model is $\tau^{\text{Rouse}} \sim N^2 = 10^4$ [30], which is 10 times slower than the active relaxation time $\tau^{\text{Active}} \sim N/f^a = 10^3$. However, for a segment of two monomers, the thermal time is 1, whereas the active time is $1/f^a = 10$. It is worth mentioning that any active force of the same order of magnitude would qualitatively give the same results as those given by $f^a = 0.1$.

B. MSD curves and input bending stiffness

To gain insights from the tangentially driven polymer model, we kept certain input parameters fixed. In our simulations, spatial dimensions were determined relative to the setup size and the average length and thickness of the worms, as detailed earlier. Activity was intentionally set to low values to ensure that the contour fluctuations of the active polymer mirrored the fluctuations observed in the worms. Subsequently, the bending stiffness was derived from the persistence length of the worms (as described above). However, due to activity and interactions with obstacles (e.g. confinement), the effective persistence length, and thus the bending stiffness of the tangentially driven polymer, deviated from the input value. The bending stiffness was adjusted to ensure that the effective persistence length matched between experiments and simulations. The values are reported below:

Setup	κ_{input}	$\kappa_{effective}$	$\kappa_{experiments}$
Free space, $\phi = 0$	9	9.0	9,17
Disordered, $\phi = 10$	10	9.5	9.36
Disordered, $\phi = 20$	10	9.5	9.31
Disordered, $\phi = 30$	11	10.5	10.95
Disordered, $\phi = 40$	13	12.0	11.95
Ordered, $\phi = 40$	7	7.0	7.17
Ordered, $\phi = 50$	5.5	6.0	6.20

In figure S12 the results from the simulations are shown, all curves are rescaled by their respective rotational decorrelation time.

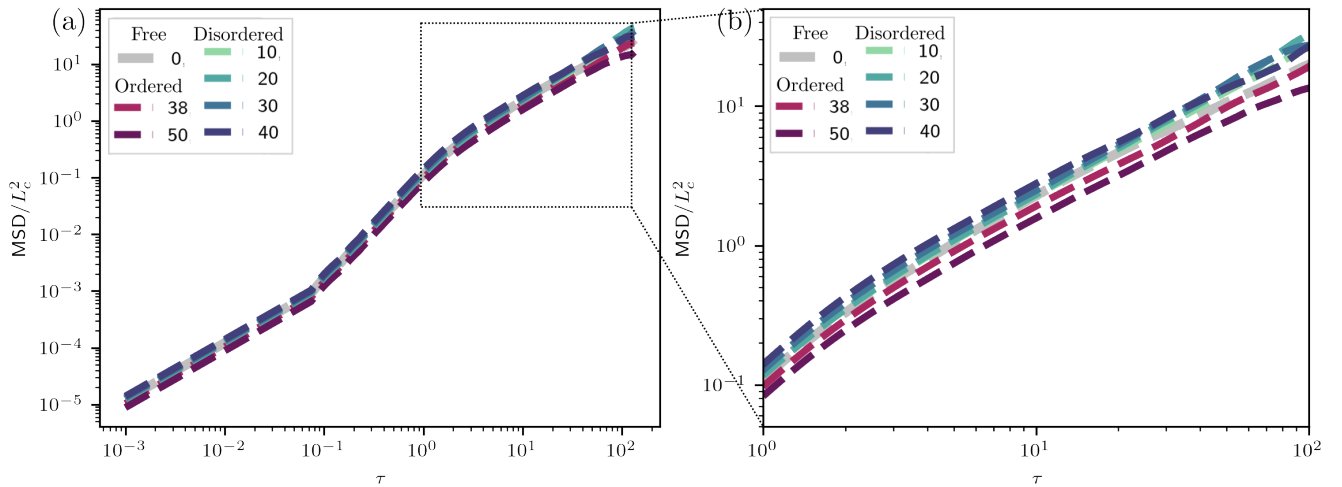


FIG. S12. **MSD results from the simulations.** (a) All simulations are done in the same geometries as the experiments, with the relevant bending stiffness and rescaled by their respective rotational decorrelation time. See table IIB for all bending stiffness used. (b) Zoom to the diffusive part of the MSD.

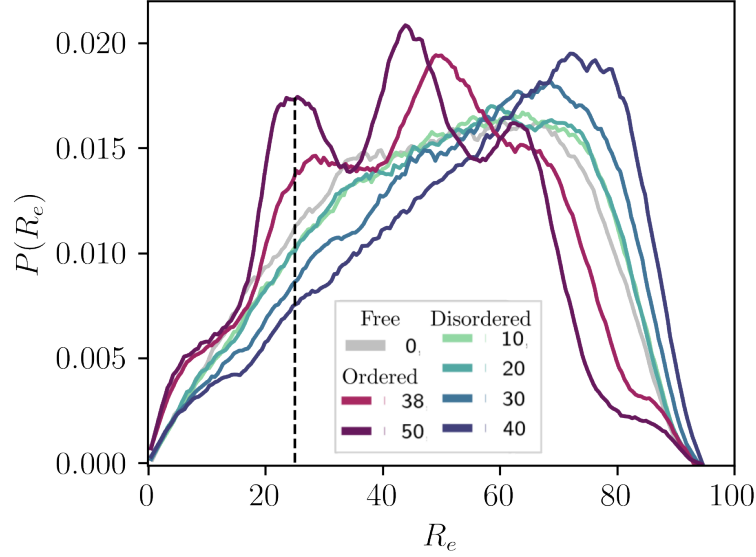


FIG. S13. **The probability distribution function of end-to-end distance of simulated polymers in different media.** The black dashed line shows the value of the first peak ($R_e = 25$) of the active polymer moving in ordered medium with $\phi = 0.5$.

C. Characterization of trapping events for simulation

We measure trapping and reptating events based on the following method for the simulated active polymers. Since for tangentially driven polymers the self propulsion velocity of the center of the mass is proportional to R_e , we use the distribution of the end-to-end distance to find the threshold on R_e below which the chain is trapped state. In Fig.S13 we have the $P(R_e)$ for all of the simulations. The most confined chain is the one in the ordered medium with $\phi = 0.5$. This particular distribution has three peaks showing the interaction of the polymer with the obstacles. We use the position of the first peak at $R_e \approx 25$ to set the threshold. We use the same value for all of the simulations for consistency. Therefore, a chain is labeled trapped when $R_e < 25$, otherwise reptating.